Kinetic-MHD hybrid simulation of fishbone modes excited by fast ions on the experimental advanced superconducting tokamak (EAST)

Cite as: Phys. Plasmas **24**, 032507 (2017); https://doi.org/10.1063/1.4978562
Submitted: 20 January 2017 • Accepted: 28 February 2017 • Published Online: 17 March 2017

Youbin Pei, Nong Xiang, Youjun Hu, et al.

Kinetic-MHD hybrid simulation of fishbone modes excited by fast ions on the experimental advanced superconducting tokamak (EAST)

Youbin Pei,[1,2,3] Nong Xiang,[1,a)] Youjun Hu,[1] Y. Todo,[4] Guoqiang Li,[1] Wei Shen,[1] and Liqing Xu[1]
[1]*Institute of Plasma Physics, Chinese Academy of Sciences, Hefei, Anhui 230031, China*
[2]*University of Science and Technology of China, Hefei, Anhui 230026, China*
[3]*Center for Magnetic Fusion Theory, Chinese Academy of Sciences, Hefei, Anhui 230031, China*
[4]*National Institute for Fusion Science, Toki, Gifu 509-5292, Japan*

(Received 20 January 2017; accepted 28 February 2017; published online 17 March 2017)

Kinetic-MagnetoHydroDynamic hybrid simulations are carried out to investigate fishbone modes excited by fast ions on the Experimental Advanced Superconducting Tokamak. The simulations use realistic equilibrium reconstructed from experiment data with the constraint of the $q = 1$ surface location (q is the safety factor). Anisotropic slowing down distribution is used to model the distribution of the fast ions from neutral beam injection. The resonance condition is used to identify the interaction between the fishbone mode and the fast ions, which shows that the fishbone mode is simultaneously in resonance with the bounce motion of the trapped particles and the transit motion of the passing particles. Both the passing and trapped particles are important in destabilizing the fishbone mode. The simulations show that the mode frequency chirps down as the mode reaches the nonlinear stage, during which there is a substantial flattening of the perpendicular pressure of fast ions, compared with that of the parallel pressure. For passing particles, the resonance remains within the $q = 1$ surface, while, for trapped particles, the resonant location moves out radially during the nonlinear evolution. In addition, parameter scanning is performed to examine the dependence of the linear frequency and growth rate of fishbones on the pressure and injection velocity of fast ions. *Published by AIP Publishing.* [http://dx.doi.org/10.1063/1.4978562]

I. INTRODUCTION

Fishbone modes are usually considered as a kind of internal kink mode destabilized by energetic particles (EPs).[1–3] In tokamaks, EPs generated by fusion reactions[4] and/or auxiliary heating can destabilize the fishbone modes,[5–7] which can cause loss of EPs,[8,9] thus reducing the efficiency of plasma heating and possibly damaging the first wall. A fishbone mode was first observed in the experiments with near perpendicular neutral beam injection (NBI) in the Poloidal Divertor eXperiments (PDX).[10] Fishbone modes have been extensively investigated both analytically and numerically for decades.[1,11–16] One of the established analytic models interpreting the fishbone mode considers the resonance between the kink mode and the motion of EPs.[1] The motion that keeps the resonance can be the toroidal precession of trapped EPs,[1] the toroidal transit motion of passing particles,[16] or the bounce motion of trapped particles.[17] A great deal of numerical simulations have been carried out to investigate the interaction between fishbone modes and EPs.[13,18–20] Early works using the reduced model and keeping the mode structure fixed found the redistribution of EPs by the mode.[21] A numerical study using the reduced MagnetoHydroDynamic (MHD) model and including the MHD nonlinearity[14] emphasized the influence of MHD nonlinearity on the mode stability and mode structure in the regime of near instability threshold and well above the threshold. Self-consistent simulations using the M3D-K code found that the frequency chirps down due to the steepest pressure gradient of the EP region moving out radially.[4]

In this work, self-consistent kinetic-MHD hybrid simulations using the MEGA code[22] are carried out to investigate the fishbone instabilities excited by fast ions on the Experimental Advanced Superconducting Tokamak (EAST). The simulations use realistic equilibrium reconstructed by the EFIT[23] code with the constraint of the $q = 1$ radial location (q is the safety factor). Anisotropic slowing down distribution is used to model the distribution of fast ions generated by deuterium NBI.

The simulation results show that, as expected, the dominant harmonic of the mode is of $m/n = 1/(-1)$ and mainly localizes within the $q = 1$ surface, where m and n are the poloidal and toroidal mode numbers, respectively. The fishbone mode found in the simulation is of high frequency, with frequency being larger than the usual precession drift fishbones. Resonance condition analysis indicates that the fishbone mode is simultaneously in resonance with the bounce motion of the resonant trapped particles and the toroidal transit motion of the resonant passing particles. Both the passing particles and trapped particles are important in destabilizing the fishbone mode. The nonlinear simulations show that the mode frequency chirps down in the nonlinear stage and the frequency chirping is found to be accompanied by the flattening of the perpendicular pressure profiles and the radial moving out of the resonant location of trapped particles. The simulation results indicate the saturation level $|\delta B_\theta/B_0| \approx 10^{-3}$, where δB_θ is the perturbed poloidal magnetic field. This saturation level is in agreement with the

a)E-mail: xiangn@ipp.cas.cn

experimental observation of fishbone modes on EAST.[24] Furthermore, the simulation results indicate that the mode saturation level is independent of the fast ion parameters in the parameter regime examined. In addition, parameter scanning is performed to examine the dependence of the linear frequency and growth rate of fishbones on the pressure and injection velocity of fast ions. The results of this parameter scanning are in qualitative agreement with those of previous studies.[4,25]

The remainder of this article is organized as follows: Sec. II describes the physics model used in the simulation. The parameters of the thermal plasma and fast ions used in this work are described in Sec. III. Linear and nonlinear simulation results are presented in Sec. IV. Sec. V presents a convergence study for the typical parameters used in the simulation. Sec. VI is a brief summary.

II. SIMULATION MODEL

MEGA is a numerical code calculating the interaction of EPs and thermal plasmas.[26–29] The code has been extensively used to study Alfvén eigenmodes (AEs) and energetic particle modes (EPMs). In MEGA, the thermal plasma is described by the nonlinear full MHD equations, which consist of the mass continuum equation

$$\frac{\partial \rho}{\partial t} = -\nabla \cdot (\rho \boldsymbol{u}) + \nu_n \nabla^2 (\rho - \rho_{\mathrm{eq}}), \tag{1}$$

the momentum equation (with the effect of EPs)

$$\rho \frac{\partial \boldsymbol{u}}{\partial t} = -\rho \boldsymbol{\Omega} \times \boldsymbol{u} - \rho \nabla \left(\frac{u^2}{2}\right) - \nabla p + \left(\boldsymbol{j} - \boldsymbol{j}_h'\right) \times \boldsymbol{B} - \nabla \times (\nu \rho \boldsymbol{\Omega}) + \frac{4}{3}(\nu \rho \nabla \cdot \boldsymbol{u}), \tag{2}$$

the Faraday's law

$$\frac{\partial \boldsymbol{B}}{\partial t} = -\nabla \times \boldsymbol{E}, \tag{3}$$

and the equation of state

$$\frac{\partial p}{\partial t} = -\nabla \cdot (p\boldsymbol{u}) - (\Gamma - 1) p \nabla \cdot \boldsymbol{u} + (\Gamma - 1)\left[\nu \rho \Omega^2 + \frac{4}{3}\nu \rho (\nabla \cdot \boldsymbol{u})^2 + \eta \boldsymbol{j} \cdot \left(\boldsymbol{j} - \boldsymbol{j}_{\mathrm{eq}}\right)\right] + \nu_n \nabla^2 (p - p_{\mathrm{eq}}), \tag{4}$$

where ρ, $\boldsymbol{u}$, and p are the mass density, fluid velocity, and pressure of the thermal plasmas, respectively, $\boldsymbol{B}$ is the magnetic field, $\mathbf{E}$ is the electric field, which is given by $\boldsymbol{E} = -\boldsymbol{u} \times \boldsymbol{B} + \eta\left(\boldsymbol{j} - \boldsymbol{j}_{\mathrm{eq}}\right)$, $\boldsymbol{j}$ is the current density, which is given by $\boldsymbol{j} = \nabla \times \boldsymbol{B}/\mu_0$, μ_0 is the vacuum magnetic permeability, $\boldsymbol{\Omega}$ is the vorticity given by $\boldsymbol{\Omega} = \nabla \times \boldsymbol{v}$, $\Gamma = 5/3$ is the adiabatic constant, η is the electric resistivity, and ν and ν_n are the artificial viscosity and diffusion coefficients chosen to maintain the numerical stability. The subscript "eq" represents the equilibrium variables, and $\boldsymbol{j}_h'$ is the current density of EPs without the contribution of the $\boldsymbol{E} \times \boldsymbol{B}$ drift (the contribution of the $\boldsymbol{E} \times \boldsymbol{B}$ drift disappears due to quasi-neutrality[28]). MHD equations (1)–(4) are solved in MEGA by using the fourth order (in both space and time) finite difference scheme in the right-handed cylindrical coordinates (R, ϕ, Z), where R is the major radius, ϕ is the usual toroidal angle, and Z is the vertical coordinate.

In MEGA, EPs are described by the drift/gyro kinetic equations (the drift-kinetic model is adopted in this work). The guiding-center orbits of EPs are followed by using the fourth-order Runge-Kutta method. The evolution of the distribution of EPs is simulated by the δf particle-in-cell method.

III. SIMULATION PARAMETERS

The equilibrium used in this work is reconstructed by the EFIT code by using the constrains from experimental diagnostics in EAST deuterium discharge #48605 at 4.624 s, where fishbone modes were observed.[24] The flux surface shape and the simulation region are shown in Fig. 1(a). The profiles of total plasma pressure P (including the contribution from fast ions), electron number density n_e, and safety factor q are shown in Fig. 1(b).

In this work, to model the fast ions generated by deuterium NBI, we use an anisotropic slowing down distribution given by

$$f_{\mathrm{eq}}\left(\bar{\psi}_p, v, \Lambda\right) = C \exp\left(-\frac{\bar{\psi}_p}{\psi_{\mathrm{scale}}}\right) \frac{1}{v^3 + v_{\mathrm{crit}}^3} \times \frac{1}{2}\mathrm{erfc}\left(\frac{v - v_{\mathrm{birth}}}{\Delta v}\right) \exp\left(-\frac{(\Lambda - \Lambda_0)^2}{\Delta \Lambda^2}\right), \tag{5}$$

where C is a constant determining the stored energy of fast ions; $\bar{\psi}_p$ is the normalized poloidal magnetic flux; ψ_{scale} is a quantity characterizing the radial gradient of fast ions; v is the velocity of fast ions; and v_{crit} is the critical velocity for

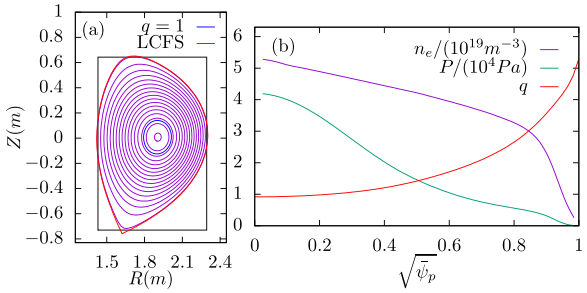

FIG. 1. (a) Magnetic surface shape of EAST discharge #48605 at 4.624 s. The Last-Closed-Flux-Surface (LCFS) and $q = 1$ surface are indicated in (a). The simulation region on the poloidal plane is also indicated in (a), which is a rectangle with $R_{\min} < R < R_{\max}$ and $Z_{\min} < Z < Z_{\max}$, where $R_{\min}$, $R_{\max}$, $Z_{\min}$, and $Z_{\max}$ are the extreme points on the flux surface with $\sqrt{\bar{\psi}_p} = 99\%$, where $\bar{\psi}_p$ is the normalized poloidal magnetic flux. (b) Radial profiles of the total pressure, safety factor, and electron number density. The radial location of the $q = 1$ surface is at $\sqrt{\bar{\psi}_p} = 0.25$. The value of the safety factor at the magnetic axis is $q_0 = 0.91$. The value of the electron number density at the magnetic axis is $n_{e0} = 5.27 \times 10^{19}\mathrm{m}^{-3}$. The toroidal magnetic field at the magnetic axis is $B_{\phi 0} = +1.75\,\mathrm{T}$. The toroidal plasma current is $I_p = -412\mathrm{kA}$. The stored energy of the plasma corresponding to the pressure profile is 175kJ.

the collisional friction of fast ions with thermal electrons and ions being equal, which is given by[30]

$$v_{\rm crit} = \left(\frac{3\sqrt{\pi}m_e}{4m_D}\right)^{1/3} v_{\rm te}, \tag{6}$$

where m_e and m_D are the masses of electrons and deuterons, respectively, $v_{\rm te}$ is the thermal velocity of electrons; $v_{\rm birth}$ is the neutral beam injection velocity; Δv is a small velocity (compared with $v_{\rm birth}$), which is used to set the cutoff width near $v_{\rm birth}$; $\Lambda = \mu B_0/\varepsilon$ is the normalized magnetic moment with μ and ε being the magnetic moment and energy of fast ions and B_0 being the magnetic filed strength at the magnetic axis; and Λ_0 and $\Delta\Lambda$ characterize the peak location and the width of the distribution over the pitch angle, respectively.

In this work, except the parameter scanning in Secs. IV D–IV F, we fix the following parameters, $\psi_{\rm scale} = 0.3$ and $v_{\rm crit} = 1.89 \times 10^6\,{\rm m/s}$, which corresponds to the critical velocity given by Eq. (6) evaluated with the electron temperature $T_e = 2\,{\rm keV}$; the injected beam velocity is chosen as $v_{\rm birth} = 2.398 \times 10^6\,{\rm m/s}$, corresponding to a deuteron with a kinetic energy of 60 keV; the cutoff width near the beam velocity is chosen as $\Delta v = 0.05 V_{A0}$, where $V_{A0} = \sqrt{B_0^2/\mu_0 n_{e0}(m_D + m_e)} = 3.7178 \times 10^6\,{\rm m/s}$ is the Alfvén velocity at the magnetic axis; n_{e0} is the electron number density at the magnetic axis; the central pitch angle variable Λ_0 is chosen as $\Lambda_0 = 0.88$, which is estimated by using the NUBEAM code;[31] and the expansion width of the distribution over Λ is chosen as $\Delta\Lambda = 0.1$. The constant C appearing in Eq. (5), which determines the stored energy of fast ions, is characterized in the following by $\beta_{h0} = p_{h0}/\left(B_0^2/2\mu_0\right)$, where p_{h0} is a constant pressure, and the spatial integration, $\int \frac{3}{2} p_{h0} \exp\left(-\bar{\psi}_p/\psi_{\rm scal}\right) d^3V$, is used to set the stored energy of fast ions given by distribution (5). We choose $\beta_{h0} = 1\%$ except in the sections of parameter scanning.

In this work, the viscosity and diffusivity are set to be $\nu = \nu_n = 10^{-5} V_{A0} R_{\rm axis}$, and the resistivity η is set to be zero, where $R_{\rm axis}$ is the major radius of the magnetic axis. The numbers of grid points used in the simulation are $(128 \times 16 \times 128)$ for cylindrical coordinates (R, ϕ, Z). Considering the computing efficiency, 2^{19} markers are used in the parameter scanning study in Secs. IV E and IV F, and 2^{22} markers are used in the other sections. A convergence test over the number of markers is presented in Sec. V, which shows that the number of markers used in this work is acceptable.

IV. SIMULATION RESULTS

A. Mode structure and frequency

The MEGA code uses the cylindrical coordinates (R, ϕ, z) to discretize the MHD equations and advance the orbits of EPs. Magnetic flux coordinates (ψ, θ, ϕ) are used when analyzing the simulation results, where ψ is a flux surface label (in this work, $\psi = \sqrt{\bar{\psi}_p}$), ϕ is the usual toroidal angle, and θ is chosen to make magnetic field lines straight on the (θ, ϕ) plane. The zero point of the θ coordinate is chosen at the low-field side (LFS) of the midplane, and the positive direction of θ is the counterclockwise direction when viewed in the ϕ direction. In (ψ, θ, ϕ) coordinates, a perturbation a can be expanded in two-dimensional Fourier series over θ and ϕ

$$a(\psi,\theta,\phi,t) = \sum_{n=-\infty}^{\infty}\sum_{m=0}^{\infty}\Big[a_{mn}^{(c)}(\psi,t)\cos(m\theta + n\phi) + a_{mn}^{(s)}(\psi,t)\sin(m\theta + n\phi)\Big], \tag{7}$$

where m and n are the poloidal and toroidal mode numbers, respectively, and $a_{mn}^{(c)}(\psi,t)$ and $a_{mn}^{(s)}(\psi,t)$ are cosine and sine parts of the Fourier expansion coefficients, respectively. A single harmonic in the Fourier expansion (7) can also be written as

$$a_{mn}^{(c)}(\psi,t)\cos(m\theta + n\phi) + a_{mn}^{(s)}(\psi,t)\sin(m\theta + n\phi) = A\cos[m\theta + n\phi - \alpha], \tag{8}$$

where A is the amplitude of the perturbation given by $A = \sqrt{\left(a_{mn}^{(s)}\right)^2 + \left(a_{mn}^{(s)}\right)^2}$ and α is the phase angle given by $\alpha = {\rm atan}\left(a_{mn}^{(s)}, a_{mn}^{(c)}\right)$. Using this, the angular frequency of the perturbation can be written as $\omega = d\alpha/dt$ and the growth rate can be written as $\gamma = d\ln(A)/dt$.

In this work, we keep only the $n = [-8, 8]$ toroidal harmonics, and higher n harmonics are filtered out every 1000 time steps in the simulation. Figure 2(a) plots the time evolution of the MHD perturbation energy of different toroidal mode numbers, which indicates that the $|n| = 1$ mode is dominant in the simulation with other n harmonics being negligibly small. Figure 2(b) plots the amplitude of the various poloidal harmonics of the $n = -1$ component of the radial velocity in the linear stage, which indicates that the $m = 1$ harmonic is dominant. The results in Fig. 2(b) also indicate that the dominant $m = 1$ harmonic is localized within the $q = 1$ surface.

Figure 2(c) plots the time evolution of the $m/n = 1/-1$ component of the poloidal magnetic field B_θ. The result shows that B_θ oscillates with a frequency $f = \omega/2\pi \approx 16.4$kHz and grows exponentially in the linear stage. In the nonlinear stage, the mode frequency chirps down rapidly from 16.4kHz in the linear stage to 6.75kHz, as shown in Fig. 2(c). Based on these observations, we identify that the dominant mode found in the simulation is a fishbone mode.

Using Eq. (8) and noting that $n < 0, m > 0$, and $\omega > 0$, the toroidal and poloidal propagation directions of the mode can be determined. Toroidally, the mode travels in the $-\phi$ direction. Poloidally, the mode travels in the $+\theta$ direction. In terms of physical quantities, the mode propagates toroidally in the co-current direction and poloidally in the ion diamagnetic drift direction. These results are consistent with the general rules for the propagation direction of ion-driven modes[32] and also the EAST experimental observation of fishbone modes.[24]

The two-dimensional structures of the perturbed toroidal electric field E_ϕ on the poloidal plane in the linear stage and nonlinear stage are plotted in Figs. 3(a) and 3(b), which

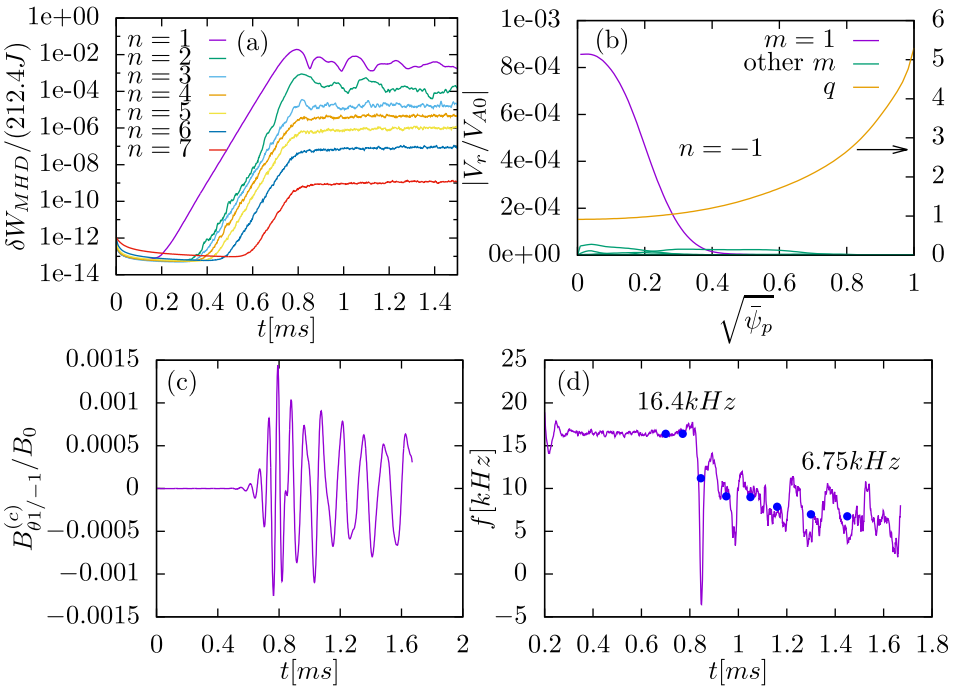

FIG. 2. (a) Time evolution of MHD perturbation energy of various toroidal harmonics. (b) Radial profiles of the amplitude of the various poloidal harmonics of the $n=-1$ component of the radial velocity in the linear stage; the profile of the safety factor is also plotted. (c) and (d) Plot of the time evolution of the cosine component and frequency of the $m/n=1/-1$ harmonic of the perturbed poloidal magnetic field B_θ. The blue dots in (d) indicate the mean frequency calculated using the period of the oscillation.

show that, as expected, the $m=1$ harmonic is dominant. Comparing Figs. 3(a) and 3(b), we find that the mode structures of the linear and nonlinear stages are different in that the twist of the mode structure in the nonlinear stage is more significant than that in the linear stage. This twisted structure is consistent with the previous fishbone simulations presented in Refs. 3 and 4. The twist may be attributed to the radial phase variation induced by the kinetic effects of the fast ions, and it has also been found in fast ions driving AE and EPM simulations.[33–35]

B. Resonance condition of fast ion and fishbone mode interactions

To identify the particles that are resonant with the fishbone mode, a simple method is used to pick out those particles that have a large value of $|\delta f|$. The large perturbation $|\delta f|$ to the distribution of fast ions may indicate that these particles are having a strong interaction with the modes. We pick out top 10 000 particles with a large value of $|\delta f|$ at $t=0.71$ms. To examine whether these particles are resonant with the mode, we calculate the poloidal and toroidal frequencies, ω_θ and ω_ϕ, of these particles and then examine

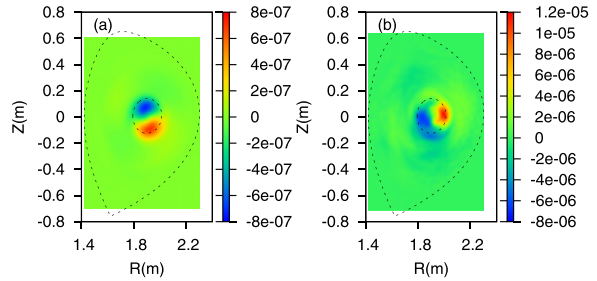

FIG. 3. Contour of the toroidal electric field E_ϕ on the poloidal plane at two time slices: (a) in the linear stage at $t=0.59$ms and (b) in the nonlinear stage at $t=1.19$ms. Also plotted on the figures are the LCFS and the $q=1$ surface.

how well the resonance condition is satisfied. The resonance condition of fast ions with a coherent mode is given by[28,36]

$$l=\frac{\omega-n\omega_\phi}{\omega_\theta}, \tag{9}$$

where ω is the mode angular frequency, n is the toroidal mode number, and l is called the resonance order in this paper and should be close to an integer if the particle is strongly resonant with the mode. Figures 4(a) and 4(b) plot the value of l calculated by Eq. (9) for the top 10 000 particles chosen above, which show that the value of $l\approx 1$ for most of the trapped particles and $l\approx 0,2$ for the passing particles. The toroidal and poloidal frequencies of trapped and passing resonant particles are plotted in Figs. 4(c) and 4(d).

For the resonant trapped particles, the resonance order $l\approx 1$, and thus Equation (9) is written as

$$\omega\approx\omega_\theta-\omega_\phi. \tag{10}$$

Further, note that, as shown in Fig. 4(c), the toroidal precession frequency of these trapped particles, ω_ϕ, is much smaller than their poloidal frequency ω_θ and thus can be dropped in Eq. (10), giving $\omega\approx\omega_\theta$, i.e., the mode frequency is approximately equal to the bounce frequency of the resonant trapped particles. This indicates that it is the bounce motion of trapped particles, instead of the precession motion, that keeps the particles in phase with the fishbone mode in this case.

For the resonant passing particles, there are two resonance orders, $l\approx 0$ and $l\approx 2$. As shown in Fig. 4(d), the number of particles with $l\approx 2$ is much less than that of particles with $l\approx 0$. For the dominant resonance order $l\approx 0$, Equation (9) is written as $\omega\approx-\omega_\phi$, i.e., the mode frequency is approximately equal to the toroidal frequency of the resonant passing particles.

The above results indicate that the mode excited in this case is simultaneously resonant with the bounce motion of

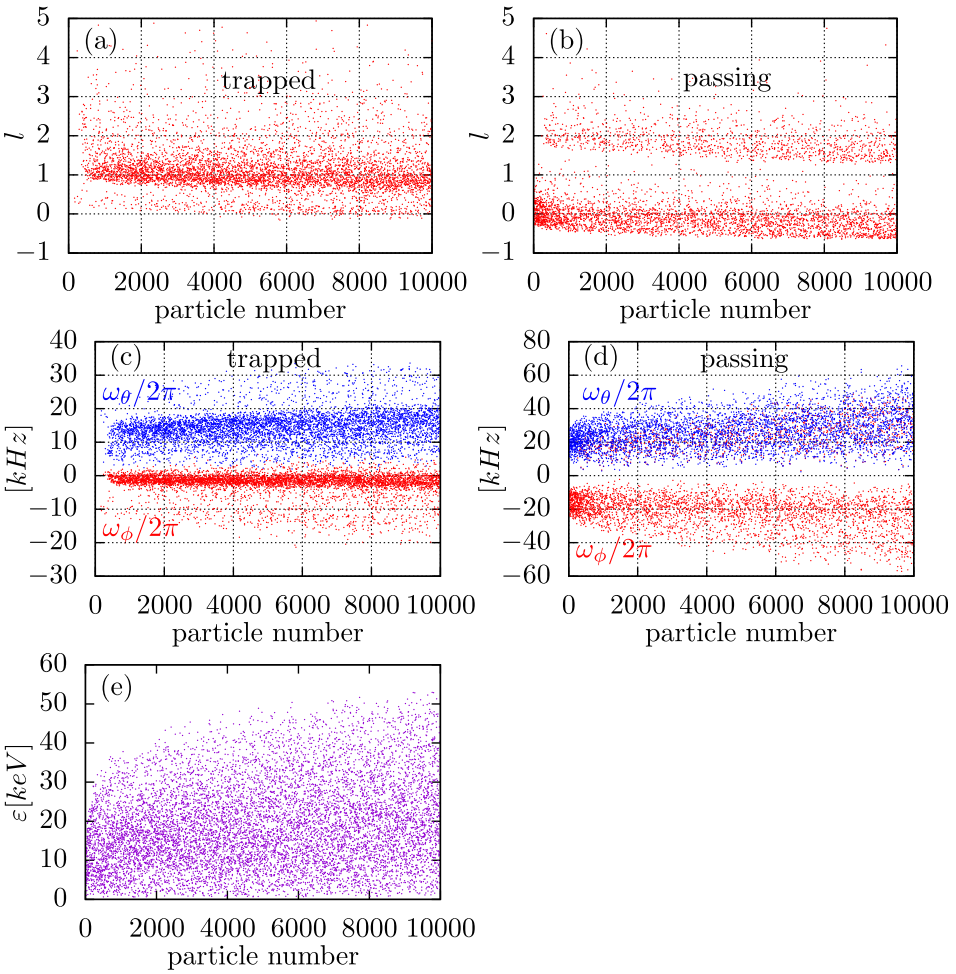

FIG. 4. (a) and (b) The values of the resonance order l of the top 10 000 markers with a large value of $|\delta f|$. Among these markers, trapped ones are shown in (a), while passing ones are shown in (b). Note that almost all of the top 200 markers are passing particles, as can be seen by comparing (a) and (b). The toroidal frequency ω_ϕ and poloidal frequency ω_θ of trapped resonant particles (c) and passing particles (d). (e) Energy of the 10 000 markers.

trapped particles and toroidal circulating motion of passing particles. The frequency of the bounce frequency of trapped particles and toroidal circulating frequency of passing particles is usually much larger than the typical toroidal precession frequency of trapped particles. Therefore, the fishbone modes simulated in this work are a kind of high-frequency fishbone mode, with frequency being larger than the usual precession drift fishbones.

The ratio of physical passing particles and trapped particles represented by the top 10 000 markers is $N_{\text{passing}}/N_{\text{trapped}} \approx 1.42$ for this case. This means that both the passing particles and trapped particles are important in destabilizing the fishbone mode.

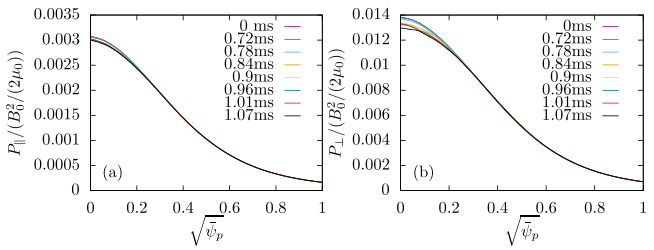

FIG. 5. Time evolution of the $m/n = 0/0$ harmonic of the parallel pressure (a) and perpendicular pressure (b) of the fast ions. The pressure is normalized by $B_0^2/2\mu_0$, where B_0 is the magnetic field strength at the magnetic axis. $t = 0.78$ms corresponds to the end of the linear stage and the beginning of the nonlinear stage.

In Fig. 4, markers are sequenced by their magnitude of $|\delta f|$ (No. 1 marker has the largest value of $|\delta f|$). Comparing Figs. 4(a) and 4(b), we find that almost all of the top 200 markers are passing particles. This indicates that the passing particles are more important than trapped ones in the interaction with the fishbone mode in our case. The reason for this can be understood by a rough estimation of the population of trapped particles within the $q = 1$ surface. The turning point of trapped particles with $\Lambda = \Lambda_0$ is located at $\mu B = \varepsilon$, where $\mu = \Lambda_0 \varepsilon / B_0$. This gives $\Lambda_0 B/B_0 = 1$. Using $B \approx B_0 R_0/R$, we have $R = \Lambda_0 R_0$. With $\Lambda_0 = 0.88$, the turning point is located at $R = 0.88R_0 = R_0 - 0.12R_0$. For the EAST tokamak, $R_0/a \approx 4$, and then $R = R_0 - 0.48a$. This indicates that the particles with $\Lambda = 0.88$ moving inside the $q = 1$ magnetic surface located at $r/a \approx \sqrt{\bar{\psi}_p} = 0.25$ do not reach the turning point. In other words, the particles inside the $q = 1$ surface with $\Lambda = 0.88$ are all passing particles, based on the zero-orbit-width approximation. This may explain why the majority of the resonant particles are passing particles. It would be interesting to investigate different q profiles with the $q = 1$ surface located at $r/a \geq 0.48$ or different fast ion distributions with Λ_0 more near unity, which may make the interaction with trapped particles dominant. This will be our near future work.

The energy of these resonant particles is plotted in Fig. 4(e), which indicates that the energy of the resonant particles is in the relatively low region ($0 \sim 30$ keV) compared with the birth energy 60 keV.

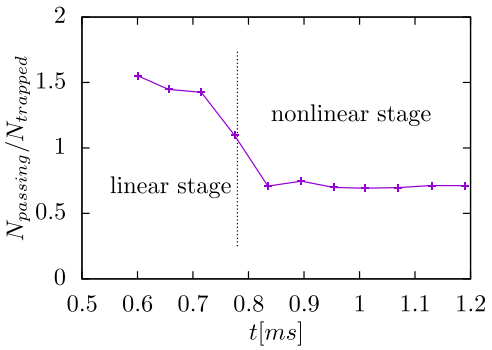

FIG. 6. Number ratio between the passing particles and trapped particles at various times.

C. Flattening of the fast ion pressure profile

Figure 5 gives the time evolution of the $m/n = 0/0$ component of the parallel and perpendicular pressure profiles of fast ions. The results indicate that the fast ion pressure profile remains unchanged in the linear stage, i.e., the fishbone mode has no significant influence on the transport of the fast ions in the linear stage. The pressure profile begins to flatten when the mode enters the nonlinear stage. In the nonlinear stage, the fast ion pressure continues flattening. The flattening mainly occurs in the core region within the $q = 1$ surface, which is consistent with the fact that the fishbone mode localizes within the $q = 1$ surface.

Figure 5 also shows that the flattening of the perpendicular pressure of fast ions is more significant than that of the parallel pressure. Note that the perpendicular pressure is mainly contributed by trapped particles and the parallel pressure is mainly contributed by passing particles. Then, the significant flattening of the perpendicular pressure may indicate that, in the saturation stage, trapped particles have a stronger interaction with the mode than the passing particles do.

To verify this, we pick out top 10 000 markers with a large value of $|\delta f|$ and then examine the number ratio between the physical passing particles and trapped particles at various times. The results are plotted in Fig. 6. The results indicate that the physical number of trapped particles exceeds that of the passing particles in the nonlinear stage. This gives evidence that trapped particles have a more significant influence on the nonlinear evolution of the mode than that the passing particles do.

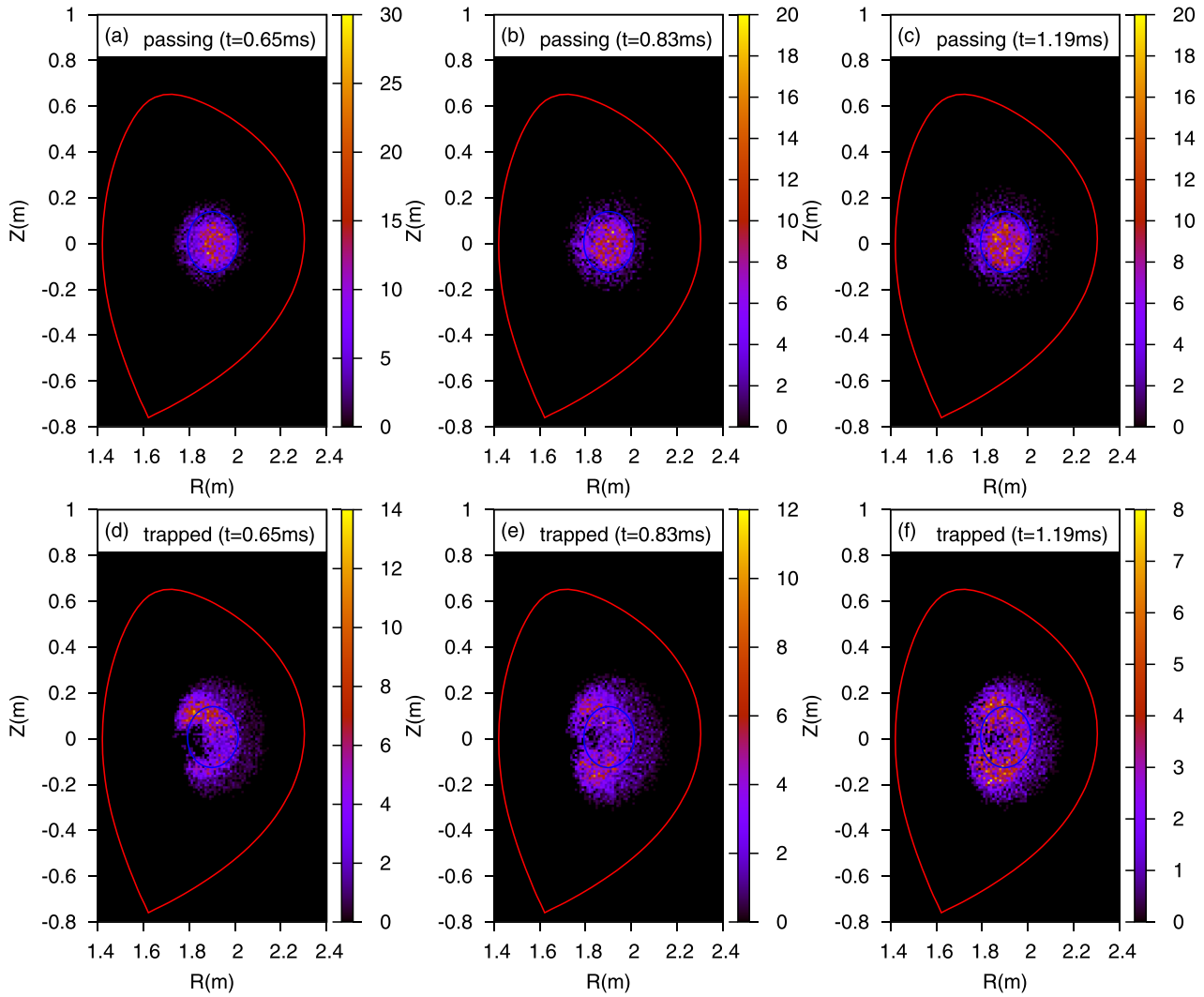

FIG. 7. Contour plots of the number density of passing particles from the physical particles represented by the top 10 000 markers with a large value of $|\delta f|$ on the poloidal plane in the (a) linear growth stage ($t = 0.65$ms), (b) initial saturation stage ($t = 0.83$ms), and (c) late stage of nonlinear evolution ($t = 1.19$ms). (d)–(f) are the same as (a)–(c), respectively, but for trapped particles. The LCFS and $q = 1$ surface are also plotted.

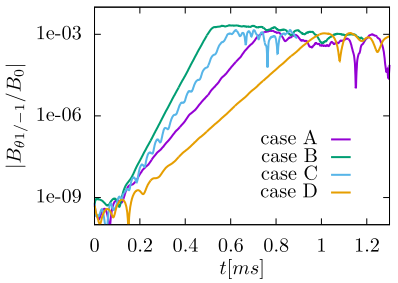

FIG. 8. Time evolution (on a logarithmic scale) of the $m/n = 1/-1$ harmonic of the perturbed poloidal magnetic field for the cases with different fast ion parameters. Case A: $\varepsilon_{\text{birth}} = 60\,\text{keV}$, $\beta_{h0} = 1.0\%$, $\Lambda_0 = 0.88$, $\psi_{\text{scale}} = 0.3$; case B: $\varepsilon_{\text{birth}} = 60\,\text{keV}$, $\beta_{h0} = 1.0\%$, $\Lambda_0 = 0.95$, $\psi_{\text{scale}} = 0.3$; case C: $\varepsilon_{\text{birth}} = 80\,\text{keV}$, $\beta_{h0} = 1.5\%$, $\Lambda_0 = 0.88$, $\psi_{\text{scale}} = 0.2$; and case D: $\varepsilon_{\text{birth}} = 60\,\text{keV}$, $\beta_{h0} = 1.0\%$, $\Lambda_0 = 0.88$, $\psi_{\text{scale}} = 0.5$.

Furthermore, for the 10 000 markers chosen above, we examine the time evolution of the spatial density of physical particles represented by these markers on the (R, Z) plane. The results are plotted in Figs. 7(a)–7(f). The results show that the resonant location of passing particles remains within the $q = 1$ surface during the fishbone evolution; however, the resonant location of trapped particles moves out radially from the linear stage (Fig. 7(d)) to the initial saturation stage (Fig. 7(e)) and the late stage of nonlinear evolution (Fig. 7(f)). This radial moving out of the resonant location of trapped particles also corresponds to the flattening of the perpendicular pressure of fast ions.

The flattening of the perpendicular pressure profile of fast ions is accompanied by the frequency chirping down process shown in Fig. 2(b). This is consistent with the conclusion in Ref. 4 that the frequency chirping is related to the radial moving out of the shoulder in trapped particle distribution.

D. Saturation level of fishbone modes

As is shown in Fig. 2(b), the saturation level of the $m/n = 1/-1$ component of the poloidal perturbed magnetic field is $|B_{\theta 1/-1}/B_0| \approx 10^{-3}$, which agrees with the EAST experimental observation.[24] To investigate the dependence of the mode amplitude saturation level on fast ion parameters, a series of parameter scans are carried out. Figure 8 shows the nonlinear amplitude evolution of the $|B_{\theta 1/-1}|$ component for cases with different fast ion parameters (beam injection energy $\varepsilon_{\text{birth}}$, central pitch angle Λ_0, beta value on magnetic axis β_{h0}, and scale length ψ_{scale}). Figure 8 shows that these fast ion parameters have little influence on the fishbone mode saturation level in this parameter regime of fast ions.

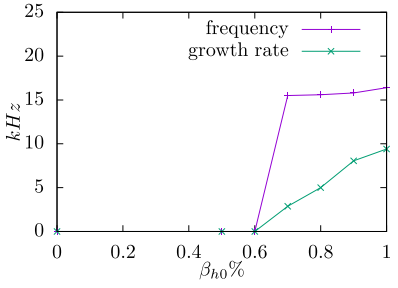

FIG. 9. The fishbone mode frequency and growth rate as functions of β_{h0} of fast ions. The mode frequency and growth rate are calculated by using the $m/n = 1/-1$ harmonic of the poloidal magnetic field, $B_{\theta 1/-1}$.

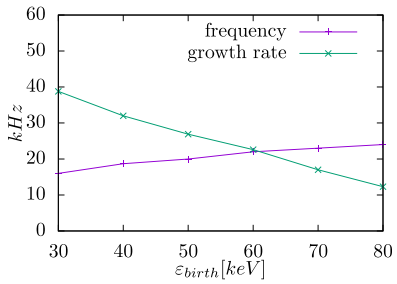

FIG. 10. The dependence of the growth rate and mode frequency on the beam injection energy $\varepsilon_{\text{birth}}$. Other parameters are fixed with $\Lambda_0 = 0.88$, $\beta_{h0} = 1.5\%$, and $\psi_{\text{scale}} = 0.3$. β_{h0} in this case is chosen to be a large value to make sure that fishbone modes are excited.

E. Dependence of the mode frequency and growth rate on fast ion beta

Figure 9 plots the fishbone mode frequency and the linear growth rate as functions of β_{h0} while fixing the scale-length ψ_{scale} and approximately fixing the total stored energy of the thermal plasma and fast ions. The results indicate that the kink mode is stable when β_{h0} is smaller than a critical value. But when β_{h0} is larger than a critical value, the fishbone mode is destabilized with a nonzero frequency. It also can be found from Fig. 9 that with increasing β_{h0}, the growth rate increases almost linearly while the real frequency of the mode is almost kept constant. The growth rate of the fishbone mode is determined by the pressure gradient of the fast ions. The pressure gradient increases with increasing β_{h0}; therefore, the growth rate increases with increasing β_{h0}. The fishbone mode frequency is determined by the characteristic orbit frequencies of the resonant fast ions, which is independent of the pressure gradient of fast ions. Thus, the mode frequency is nearly unchanged with increasing β_{h0}. These numerical results are consistent with the previous numerical and analytical results.[1,4,14]

F. Dependence of the linear growth rate and frequency on beam velocity

The beam injection velocity is an important parameter in determining the properties of fishbone modes. Figure 10 shows the dependence of the mode frequency and growth rate on the beam injection energy $\varepsilon_{\text{birth}}$. The results indicate that the frequency increased with increasing $\varepsilon_{\text{birth}}$. This can

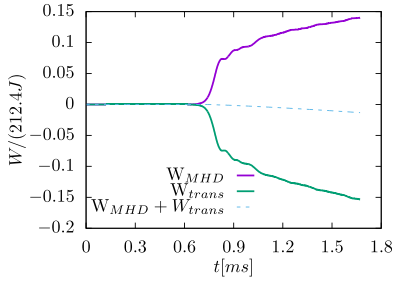

FIG. 11. Time evolution of the total MHD fluctuation energy W_{MHD} and the energy transferred from the bulk plasmas to fast ions W_{trans}. The dashed line represents the sum of the W_{MHD} and W_{trans}.

be understood by noting that the mode frequency is determined by the characteristic orbit frequency of fast ions, which usually increases with increasing birth energy.

The results show that the growth rate of the fishbone mode decreases with increasing $\varepsilon_{\text{birth}}$. This trend is not well understood. It is possibly due to that the higher frequency modes may be more near the Alfvén continuum and thus encounter larger continuum damping. This trend is in agreement with the M3D-K simulation result using the same EAST equilibrium, which will be reported in our future publication. Similar results based on other tokamaks are also obtained in previous works.[2,3,25]

G. On energy conservation

The total MHD fluctuation energy is given by[27]

$$W_{\text{MHD}} = \int \left(\frac{1}{2}\rho \boldsymbol{u}^2 + \frac{\boldsymbol{B}^2 - \boldsymbol{B}_{\text{eq}}^2}{2\mu_0} + \frac{\delta p}{\Gamma - 1} \right) dV, \tag{11}$$

where $\boldsymbol{B}_{\text{eq}}$ is the equilibrium magnetic filed and δp is the perturbed pressure of the thermal plasma. The energy transferred from the thermal plasma to fast ions is written as

$$W_{\text{trans}} = \int_0^t dt' \int \boldsymbol{j}_h{}' \cdot \boldsymbol{E} dV. \tag{12}$$

Figure 11 plots the time evolution of W_{MHD} and W_{trans}, which indicates that the energy transferred from the fast ions to the bulk plasma, $-W_{\text{trans}}$, is approximately equal to the total fluctuation MHD energy, W_{totalMHD}. This indicates that the energy conservation is preserved well in the simulation.

V. CONVERGENCE STUDY

Considering the computing efficiency, the typical number of markers used in this paper is 2^{19} for the linear cases presented in Secs. IV E and IV F and 2^{22} for the nonlinear evolution cases presented in the other sections. In order to confirm the simulation results, the convergence study is carried out with regard to the number of markers. Two cases with different numbers of markers, 2^{19} markers vs. 2^{22} markers, are compared in Fig. 12, which indicates that the linear growth rate and frequency in these two cases are almost the same. This indicates that the numerical convergence is sufficient for the number of markers used in this paper.

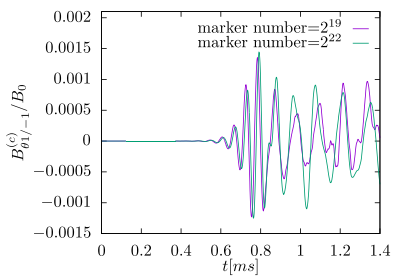

FIG. 12. Comparison of the time evolution of the cosine part of the perturbed poloidal magnetic field $B_{\theta 1/-1}$ between two cases with different numbers of markers, 2^{19} markers, and 2^{22} markers. The spatial grids for the two cases are the same [$(128 \times 16 \times 128)$ grid points in (R, ϕ, Z) coordinates].

VI. SUMMARY

Kinetic-MHD hybrid simulations using the MEGA code are carried out to investigate the fast ion driven fishbone instabilities on the EAST tokamak, using the equilibrium reconstructed by the EFIT code from the experiment data. The fishbone mode found in the simulation is a kind of high-frequency fishbone mode with frequency larger than the toroidal precession frequency of trapped particles. The resonance condition is used to identify resonant particles, which shows that the fishbone mode is mainly resonant with the poloidal bounce motion of the resonant trapped particles and the toroidal transit motion of the resonant passing particles. The results show that the number of resonant passing particles is comparable with that of the resonant trapped particles, which indicates that both trapped and passing particles are important in driving the mode.

The mode frequency chirps down as the mode reaches saturation. In the nonlinear stage, the number of trapped particles exceeds that of the passing particles. There is a significant flattening of the perpendicular pressure in the nonlinear stage, which is related to the radial moving out of the resonant location of trapped particles. The flattening of the parallel pressure is very small, and there is no obvious radial moving out of the resonant location of passing particles. These results may indicate that trapped particles have a more significant influence on the mode than that the passing particles do in the nonlinear stage. The saturation level of the mode is on the order of $|\delta B_\theta / B_0| \approx 10^{-3}$, which agrees with the experimental observations. Furthermore, parameter scanning shows that the saturation level is almost independent of the fast ion parameters examined. The twist of the two-dimension mode structure on the poloidal plane is also observed in the nonlinear stage. In addition, parameter scans indicate that the dependence of the linear frequency and growth rate on the pressure and birth velocity of fast ions is in qualitative agreement with that of previous studies.

The original motivation of this work is to reproduce, using the MEGA code, the fishbone modes observed in EAST experiments. The results indicate that this attempt is only partially successful. The mode observed in experiments is of low-frequency (5 kHz in plasma frame), which belongs to the precession resonance fishbone modes.[24] However, the mode found in our simulations is of higher frequency (16 kHz), which is proved to be related to the bounce and transit resonance. It is still unclear why the simulation shows the bounce and transit resonance instead of the precession resonance observed in the experiments. A plausible reason for this discrepancy can be that, without an experimental determination of the beam distribution, the distribution function (Eq. (5)) adopted in this work may deviate significantly from the realistic beam distribution in the experiment. Investigating the sensitivity of fishbone modes to the forms of beam distribution is one work among our future plans.

ACKNOWLEDGMENTS

Y. Pei acknowledges useful discussions with F. Wang, H. Wang, W. Chen, and J. Zhu. Numerical computations were performed on the ShenMa High Performance Computing Cluster at the Institute of Plasma Physics,

Chinese Academy of Sciences. This work was partially supported by the JSPS-NRF-NSFC A3 Foresight Program in the field of Plasma Physics (NSFC No. 11261140328), the National Magnetic Confinement Fusion Science Program of China under Grant No. 2013GB112010, and the National Natural Science Foundation of China under Grant No. 11475220.

[1]L. Chen, R. B. White, and M. N. Rosenbluth, Phys. Rev. Lett. **52**, 1122 (1984).
[2]F. Porcelli, Plasma Phys. Controlled Fusion **33**, 1601 (1991).
[3]F. Wang, G. Y. Fu, J. A. Breslau, and J. Y. Liu, Phys. Plasmas **20**, 102506 (2013).
[4]G. Y. Fu, W. Park, H. R. Strauss, J. Breslau, J. Chen, S. Jardin, and L. E. Sugiyama, Phys. Plasmas **13**, 052517 (2006).
[5]W. Chen, X. Ding, Y. Liu, G. Yuan, Y. Zhang, Y. Dong, X. Song, J. Zhou, X. Song, W. Deng, Q. Yang, X. Ji, X. Duan, Y. Liu, and HL-2A Team, Nucl. Fusion **49**, 075022 (2009).
[6]W. Heidbrink and G. Sadler, Nucl. Fusion **34**, 535 (1994).
[7]F. Zonca, P. Buratti, A. Cardinali, L. Chen, J. Q. Dong, Y. X. Long, A. Milovanov, F. Romanelli, P. Smeulders, L. Wang, Z. T. Wang, C. Castaldo, R. Cesario, E. Giovannozzi, M. Marinucci, and V. P. Ridolfini, Nucl. Fusion **47**, 1588 (2007).
[8]R. B. White, R. J. Goldston, K. McGuire, A. H. Boozer, D. A. Monticello, and W. Park, Phys. Fluids **26**, 2958 (1983).
[9]A. Fasoli, C. Gormenzano, H. Berk, B. Breizman, S. Briguglio, D. Darrow, N. Gorelenkov, W. Heidbrink, A. Jaun, S. Konovalov, R. Nazikian, J. M. Noterdaeme, S. Sharapov, K. Shinohara, D. Testa, K. Tobita, Y. Todo, G. Vlad, and F. Zonca, Nucl. Fusion **47**, S264 (2007).
[10]K. McGuire, R. Goldston, M. Bell, M. Bitter, K. Bol, K. Brau, D. Buchenauer, T. Crowley, S. Davis, F. Dylla, H. Eubank, H. Fishman, R. Fonck, B. Grek, R. Grimm, R. Hawryluk, H. Hsuan, R. Hulse, R. Izzo, R. Kaita, S. Kaye, H. Kugel, D. Johnson, J. Manickam, D. Manos, D. Mansfield, E. Mazzucato, R. McCann, D. McCune, D. Monticello, R. Motley, D. Mueller, K. Oasa, M. Okabayashi, K. Owens, W. Park, M. Reusch, N. Sauthoff, G. Schmidt, S. Sesnic, J. Strachan, C. Surko, R. Slusher, H. Takahashi, F. Tenney, P. Thomas, H. Towner, J. Valley, and R. White, Phys. Rev. Lett. **50**, 891 (1983).
[11]R. Betti and J. P. Freidberg, Phys. Rev. Lett. **70**, 3428 (1993).
[12]B. Coppi and F. Porcelli, Phys. Rev. Lett. **57**, 2272 (1986).
[13]C. C. Kim and NIMROD Team, Phys. Plasmas **15**, 072507 (2008).
[14]A. Ödblom, B. N. Breizman, S. E. Sharapov, T. C. Hender, and V. P. Pastukhov, Phys. Plasmas **9**, 155 (2002).
[15]F. Wang, G. Fu, and W. Shen, Nucl. Fusion **57**, 016034 (2017).
[16]S. Wang, Phys. Rev. Lett. **86**, 5286 (2001).
[17]E. Fredrickson, L. Chen, and R. White, Nucl. Fusion **43**, 1258 (2003).
[18]J. McClenaghan, Z. Lin, I. Holod, W. Deng, and Z. Wang, Phys. Plasmas **21**, 122519 (2014).
[19]M. Cole, A. Mishchenko, A. Könies, R. Kleiber, and M. Borchardt, Phys. Plasmas **21**, 072123 (2014).
[20]G. Vlad, S. Briguglio, G. Fogaccia, F. Zonca, V. Fusco, and X. Wang, Nucl. Fusion **53**, 083008 (2013).
[21]J. Candy, H. L. Berk, B. N. Breizman, and F. Porcelli, Phys. Plasmas **6**, 1822 (1999).
[22]Y. Todo, T. Sato, K. Watanabe, T. H. Watanabe, and R. Horiuchi, Phys. Plasmas **2**, 2711 (1995).
[23]L. Lao, H. S. John, R. Stambaugh, and W. Pfeiffer, Nucl. Fusion **25**, 1421 (1985).
[24]L. Xu, J. Zhang, K. Chen, L. Hu, E. Li, S. Lin, T. Shi, Y. Duan, and Y. Zhu, Phys. Plasmas **22**, 122510 (2015).
[25]X. Q. Wang, R. B. Zhang, L. Qin, and X. G. Wang, Plasma Phys. Controlled Fusion **56**, 095013 (2014).
[26]Y. Todo, Phys. Plasmas **13**, 082503 (2006).
[27]Y. Todo, H. Berk, and B. Breizman, Nucl. Fusion **50**, 084016 (2010).
[28]Y. Todo and T. Sato, Phys. Plasmas **5**, 1321 (1998).
[29]Y. Shiozaki and Y. Todo, J. Plasma Fusion Res. Ser. **6**, 618 (2004).
[30]ITER Physics Basis Editors, Nucl. Fusion **39**, 2471 (1999).
[31]A. Pankin, D. McCune, R. Andre, G. Bateman, and A. Kritz, Comput. Phys. Commun. **159**, 157 (2004).
[32]Y. Todo, AIP Conf. Proc. **1478**, 141 (2012).
[33]W. Zhang, I. Holod, Z. Lin, and Y. Xiao, Phys. Plasmas **19**, 022507 (2012).
[34]R. Ma, F. Zonca, and L. Chen, Phys. Plasmas **22**, 092501 (2015).
[35]Y. Hu, Y. Todo, Y. Pei, G. Li, J. Qian, N. Xiang, D. Zhou, Q. Ren, J. Huang, and L. Xu, Phys. Plasmas **23**, 022505 (2016).
[36]J. Zhu, G. Y. Fu, and Z. W. Ma, Phys. Plasmas **20**, 072508 (2013).